Binder-free Additive Manufacturing of Ceramics using Hydrothermal-assisted Jet

**Fusion** 

Fan Fei, <sup>1</sup> Levi Kirby, <sup>1</sup> Alexander Gralczyk, <sup>1</sup> Xuan Song <sup>1\*</sup>

<sup>1</sup> Industrial and systems engineering, Iowa Technology Institute, University of Iowa, Iowa City IA 52242

\*Corresponding author: xuan-song@uiowa.edu

**Abstract** 

Ceramic additive manufacturing (AM) typically uses a high fraction of organic binders to form pre-

sintered green parts that require a post de-binding process to remove. The de-binding process inevitably

results in severe gas expansion and residual chars, leading to structural defects, accumulated stress, and

compromised material properties in the final parts. Here we report a binder-free additive manufacturing

process named hydrothermal-assisted jet fusion (HJF) that utilizes a hydrothermal method to create

geometrically and compositionally complex ceramics under mild temperatures. The HJF process employs

a selectively deposited volatile dissolving ink, high pressure, and milt heat to strategically fuse a ceramic

powder bed into complex geometries. Compared to traditional AM methods for ceramics, the HJF process

eliminates the need for organic binders in green part fabrication and offers the potential to directly co-

print ceramics with other dissimilar materials, such as polymers and metals, enabling the development of

novel multi-functional ceramic composites.

Keywords: additive manufacturing, ceramics, water-based binder, mild temperature, hydrothermal

1. Introduction

Additive manufacturing (AM) technologies have proved to be a powerful tool to create ceramics with

complex geometries, which are extremely difficult to achieve using traditional machining processes due

to their inherent brittleness [1]. Primary AM processes for ceramics, such as stereolithography (SL) [2-4],

binder jetting (BJ) [5, 6], direct ink writing (DIW) [7, 8], and laminated object manufacturing (LOM) [9],

utilize organic binders, usually with a higher fraction than those in conventional ceramic processing [1],

to bond ceramic particles into green bodies before the parts are further de-binded and sintered into pure,

dense components. The use of organic binders inevitably results in severe gas expansion and residual chars during the de-binding process [10, 11], leading to structural defects (e.g., carbon retention, cracking, blistering, warping, etc.), accumulated stress [12-14], and compromised material properties (e.g., higher porosity, smaller strength, etc.) [15, 16] in the final parts. Some emerging AM methods for ceramics, e.g., direct selective laser sintering/melting [17-19], use a high-power energy beam to directly bond ceramic particles together without the need for organic binders. However, due to high thermal gradients and inherent brittleness of ceramics, many challenges still exist in using those techniques to fabricate complex ceramic structures, such as thermal shock cracking, residual stress, and low density [20]. Unlike human-made engineering ceramics, sedimentary rocks (a natural form of ceramics) in nature are formed from loose sediment particles through long-term geological accumulation and consolidation that do not involve any synthetic binders but solely rely on groundwater, mild temperature, and high pressure [21]. This binder-free rock formation process is known as lithification, as depicted in Fig.1a. The lithification process is initialized when the surface water diffuses into the sediment particles on the top of a riverbed, forming a clast-water mixture (Fig. 1b). As more sediment particles in the top layers are saturated by water, the sediment particles in deeper locations are rearranged due to the intense pressing weight of overlying sediments, resulting in a compacted clast-water mixture (Fig.1c) [22]. After that, the clast-water mixture is bonded together via a cementation process, where the groundwater carries dissolved minerals into the empty spaces between the loose particle sediments, and the dissolved minerals crystalizes between the sediment grains after the groundwater evaporates [21, 22], as shown in Fig.1d. A dense rock is formed after all the pores between the sediment particles are filled with the precipitated minerals (Fig.1e).

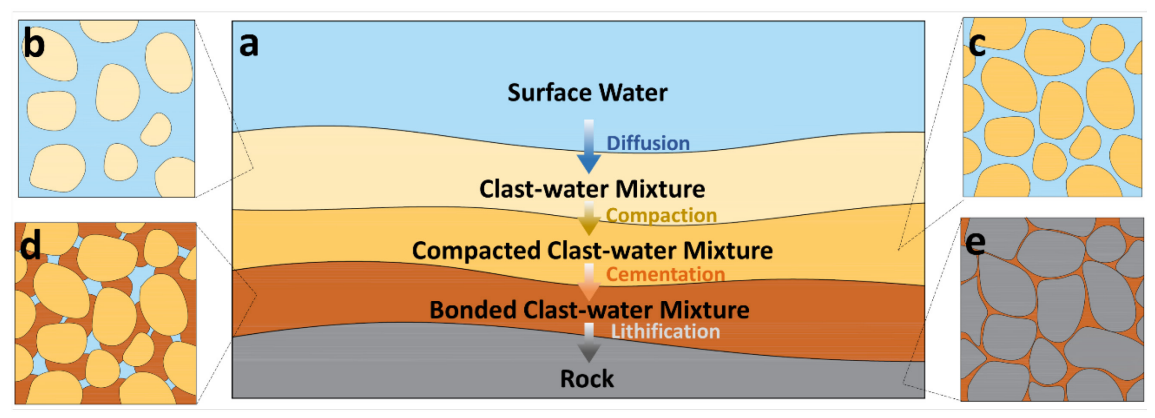


Fig.1 Schematic representation of the lithification process in nature. a. The lithification process of rocks; b. The microstructure of a clast-water mixture under the surface water where water diffusion occurs and occupies the gaps between the loose sand sediments; c. The microstructure of a compacted clast-water mixture in deeper locations underground where the sand sediments get closer to each other because of the compaction force from the overlying sediments; d. The microstructure of a bonded clast-water mixture in even deeper locations underground where the sand sediments connect to each other by cements because of the cementation process; e. The microstructure of the rock at the bottom of the ground where the water disappears, and cements occupy all the gap areas between the sediments.

Inspired by the lithification process in nature, we propose a binder-free ceramic AM process, named hydrothermal-assisted jet fusion (HJF), as depicted in Fig 2. Compared to traditional AM methods for ceramics, the HJF process eliminates the need for organic binders in green part fabrication and thus can achieve ceramic parts with higher green density and reduced defects, enabling wider adoption of ceramic AM technologies in applications such as high-ionic-conductivity batteries [23-26], microwave dielectric ceramics [27-30], piezoelectric ceramics [31-36], optical ceramic films [37, 38], etc. Meanwhile, the HJF process offers the potential to directly print ceramics with other dissimilar materials, such as polymers, enabling the development of novel biomimetic, multi-functional composites.

In this paper, we present the operating principle of the HJF process and illustrate the fundamental mechanism that governs particle fusion and densification in HJF using numerical modeling. To better understand the mass transfer process in HJF, the effects of different process parameters (including

compaction pressure, ink saturation level, temperature) on the microstructures and macroscopic properties (including density, compressive strength, dielectric property) of HJF-printed parts are studied in Section 3.1 and 3.2; a level-set-based numerical model is established to explain the hydrothermal-mediated particle fusion mechanism during the HJF process, as detailed in Section 3.3; complex three-dimensional (3D) models and patch antennas consisting of integrated dissimilar materials including ceramics, metals and polymers were printed and tested in Section 3.4. A discussion about the materials suitable for HJF and a comparison of HJF with other major AM processes are presented in Section 4.

#### 2. Material and Methods

#### 2.1 Materials

The HJF process can be applied to a wide range of ceramics that can be partially dissolved in water, or alternatively can be synthesized through wet-chemical approaches [39, 40]. In this work, we select Li<sub>2</sub>MoO<sub>4</sub> (Lithium molybdate, 99+%, Alfa Aesar, Haverhill, MA, United States, melting point 705 °C [41]) as a model material to demonstrate the capability of the HJF process in printing high-density ceramics. These materials feature excellent electrical properties, such as low dielectric loss, and have wide applications in sensing, actuation, and communication [42-47]. In the original commercial Li<sub>2</sub>MoO<sub>4</sub> powder, at least 95% of the particles were smaller than 500 μm [48]. The powder was sieved with a mesh size of 250 μm to meet the requirement of layer thickness (<=400 μm). The theoretical density of Li<sub>2</sub>MoO<sub>4</sub> is 3.07 g/cm3, and the apparent density of the Li<sub>2</sub>MoO<sub>4</sub> powder is ~58.91% with respect to the theoretical density. Deionized (DI) water was used as the printing ink for fabricating Li<sub>2</sub>MoO<sub>4</sub> specimens via the HJF process.

## 2.2 Printing apparatus and fusion mechanism

The printing apparatus for the proposed HJF process is demonstrated in Fig 2a. The system consists of a compaction piston, a piezoelectric printhead, thermal resistors, thermocouple, and other components that can be found in a standard powder-bed AM process (e.g., a roller, the x-y-z stages). The compaction piston is used to compact the ceramic particles in the powder bed at a controlled pressure. Thermal

resisters and a thermocouple were installed inside the chamber wall around the powder bed to evaporate the volatile ink under a controlled temperature.

In the HJF process, a loose ceramic powder is firstly spread into a thin layer on top of a building platform by a rotating roller (Fig 2b). A uniaxial pressure (e.g., 1-50 MPa) is then applied to the surface of the powder bed to compact the particles (Fig 2c). Following that, DI water is selectively deposited as the printing ink into the powder bed via an inkjet printhead (Fig 2d). These three steps are repeated until a complete 3D model is finished. Finally, the whole powder bed is heated under a mild temperature, e.g., 50 °C, to evaporate the water ink and trigger the fusion between the particles in the wetted region (Fig 2e). A complex ceramic part is finally obtained after removing the loose powder surrounding the bonded articles. The part can be further sintered in a furnace for a higher density.

Fig 2b1-e1 describe the microstructure evolution in a printed part during the HJF process, which is driven by a hydrothermal-mediated dissolution-diffusion-precipitation process. When a thin layer of ceramic particles is spread onto the platform, the particles are loosely packed together (Fig 2b1). A layerwise compaction force applied to the newly spread layer mechanically rearranges the particles and induces close contacts between the particles (Fig 2c1). As the water-based ink is deposited into the compacted layer, the surfaces of the ceramic particles partially dissolve in the ink (indicated by the dark orange color in Fig 2d1) under the effect of interparticle stresses. Due to a large difference in chemical potential, the dissolved species diffuse from the interparticle contact point to the pore areas, and, as the water ink is evaporated under a mild heating temperature, precipitates form at the interparticle contact point. This contributes to the fusion of the particles (Fig 2e1).

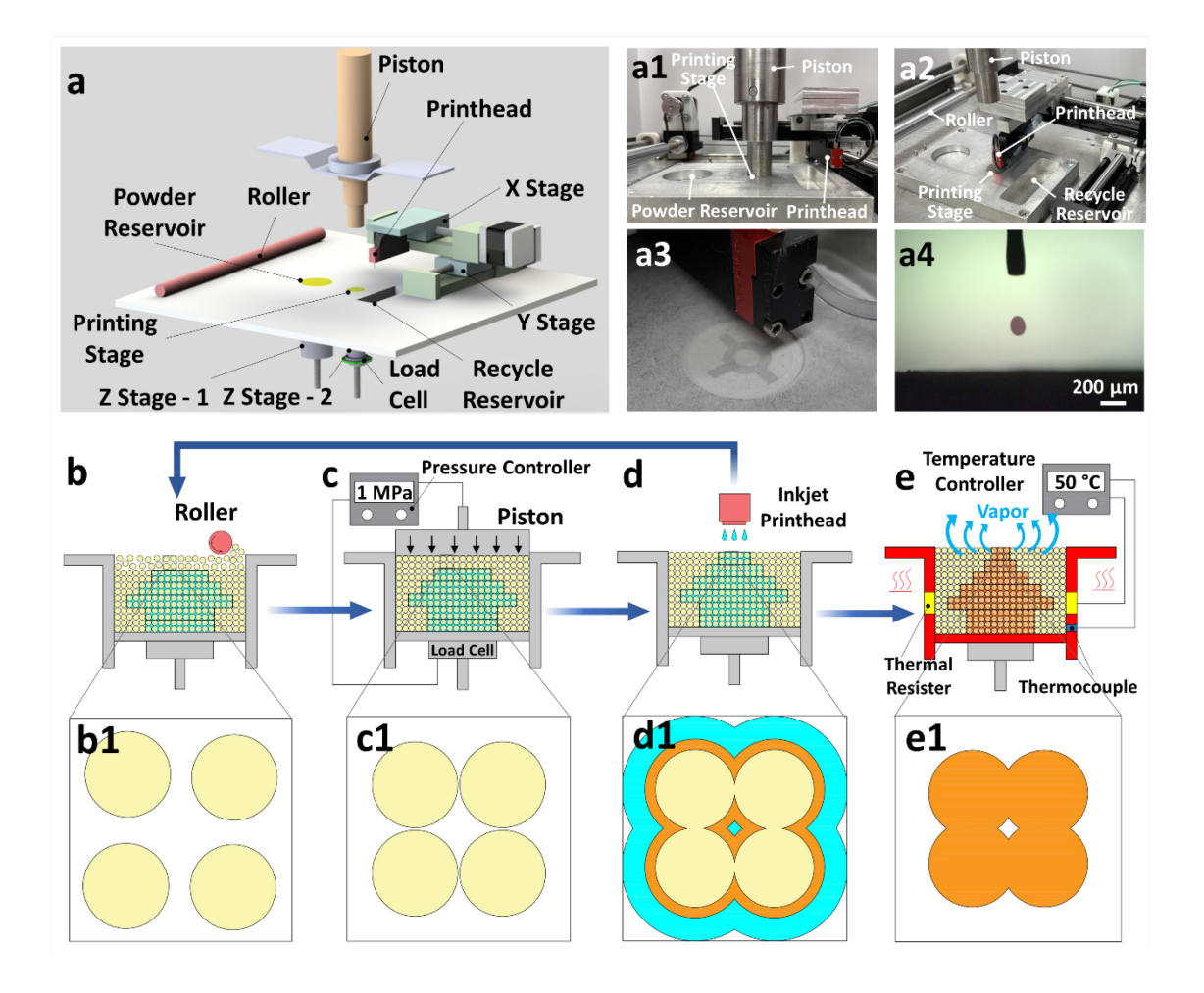


Fig 2 a. The HJF process: a1. A piston compacts the powder bed in the printing process; a2. The piston is released, and a printhead deposits a volatile dissolving ink above the printing stage; a3. Zoom-in view of the powder bed in the printing stage with a complex pattern jetted by the printhead; a4. An ink droplet captured by a high-speed camera system. Schematics of the printing process and microstructure evolution: b. A ceramic powder is spread by the roller to form a new layer; b1. Loosely packed ceramic particles; c. A compaction pressure is applied to the powder bed; c1. Closely compacted ceramic particles; d. DI water is selectively jetted into the compacted new layer; d1. Water-saturated particles with their surfaces partially dissolved in the ink; e. The powder bed is heated to evaporate the water ink; e1. Fused particles after water evaporation.

#### 2.3 Fabrication

# 2.3.1 Specimens

To study the relationships between the process parameters including compaction pressure and ink saturation level and the microstructures and macroscopic properties of HJF-printed parts, specimens were manually created by die-pressing a mixture of ceramic powder (i.e., Li<sub>2</sub>MoO<sub>4</sub>) and DI water. The specimens were fabricated in a cylindrical shape with a diameter of 20 mm and a thickness of 2 mm. The ceramic powder and the water ink were uniformly mixed at varying ink saturation levels (the weight ratio between the ink and the saturated ceramic powder) using a pestle and a mortar. A cylinder die with an internal diameter of 20 mm was used to press the mixture, and an electric hydraulic press machine (YLJ-E30T, MTI Corporation, Richmond, CA, United States) was used to press the die with a controlled compaction pressure. After compaction, the specimens were heated in an oven at 120 °C for 3 hours to evaporate the water in them.

## 2.3.2 Complex 3D structures

Specimens with more complex shapes were produced from Li<sub>2</sub>MoO<sub>4</sub> using a printing apparatus shown in Fig 2a. The machine selectively delivers a volatile dissolving ink into the powder bed via a piezoelectric inkjet head (PipeJet, BioFluidix GmbH, Breisgau, Germany). The nozzle size used in the inkjet head was 150 μm. The stroke value, which determines the deformation of the nozzle in the inkjet head, was 10 μm. The jetting velocity of the nozzle was 125 μm/ms. The layer thickness before compaction was 480 μm (Fig 2b). A compaction pressure of 1 MPa was applied to the powder bed during the printing process (Fig 2c). After the printing steps were completed (Fig 2b-d), the whole powder bed was heated at 120 °C for 3 hours to evaporate the liquid inside the particles (Fig 2e).

#### 2.3.3 Patch antennas

Circular patch antenna: A dielectric layer was fabricated from Li<sub>2</sub>MoO<sub>4</sub> using the same procedure mentioned in Section 2.3.1. A compaction pressure of 150 MPa and an ink saturation level of 15 wt.% were selected. A disk with a diameter of 20 mm and a thickness of 1.9 mm was created. Circular copper

tapes with a diameter of 12 mm and 20 mm were attached to the top and bottom sides of the disk, respectively. A SubMiniature version A (SMA) port was soldered onto the copper tapes.

Origami patch antenna: An origami antenna was designed, which consists of 6 pieces of Li<sub>2</sub>MoO<sub>4</sub> square blocks (length 3.5 mm, thickness 1.2 mm) as the dielectric layer, as shown in Fig.8a. These square blocks were arranged in a crossing shape with an overall length of 18 mm and a width of 12.5 mm. The distance between two neighboring square blocks is 1 mm (Fig.8a1). A compaction pressure of 1 MPa and an inkjet stroke value of 10 μm were applied in the printing process, following the printing procedure in Fig 2b-d. The layer thickness was initially set as 400 μm before compaction, and each layer was subsequently compressed to a thickness of 300 μm during the compaction process. A crossing-shaped copper foil with the same size as the dielectric layer was embedded in the print as the ground layer. A layer of silver conductive paint was applied between the copper foil and the Li<sub>2</sub>MoO<sub>4</sub> substrate to enhance their electrical conductivity. Six pieces of Nylon square blocks (length 3.5mm, thickness 0.5 mm) were printed on the bottom layer as the protection layer. Another crossing-shaped copper foil (internal width 2 mm, overall length 36 mm, overall width 25 mm) was attached to the other side of the dielectric layer as the patch layer for the antenna. The overall length and width were twice as large as those of the dielectric layer to provide sufficient space for folding the origami antenna.

#### 2.4 Characterization

## 2.4.1 Microstructure and density

The microstructures of the specimens were characterized by examining their fractured surfaces using a scanning electron microscope (SEM, S-3400N, Hitachi, Ibaraki, Japan). The densities of the Li<sub>2</sub>MoO<sub>4</sub> specimens were measured by the Archimedes' method, and a theoretical density of 3.07 g/cm<sup>3</sup> was used to calculate the specimens' relative densities. Since Li<sub>2</sub>MoO<sub>4</sub> is dissolvable in water, 99% isopropyl alcohol was used to do the density measurement, and its true density of 0.786 g/cm<sup>3</sup> was used in the density calculation.

## 2.4.2 Compressive strength

The compressive strengths of the specimens were tested with a universal testing machine (100 Series, TestResources, Shakopee, MN, United States), following ASTM C1424. The compressive strength  $\sigma_c$  was calculated using the equation  $\sigma_c = \frac{F_c}{A}$ , where  $F_c$  is the compressive force when the specimen fractures, and A is the calculated area of the bearing surface of the specimen.

## 2.4.3 Dielectric properties

The top and bottom sides of the specimens were coated with silver conductive paint (842AR, M.G. Chemicals, Burlington, Ontario, Canada) using a brush and cured in an oven at 65°C for 30 min. Dielectric loss (tan  $\delta$ ) and relative permittivity ( $\varepsilon_r$ ) of the silver-coated specimens were measured by a LCR meter (TH2811D, Tonghui Electronic Co. Ltd., Changzhou, China) at frequencies of 100, 1000, and 10000 Hz.

#### 2.4.4 Return loss S11

The antenna samples were powered by a 20 GHz RF signal generator (83752A, Agilent Technologies, Santa Clara, CA, United States) through an 18 GHz directional coupler (4226 Directional Coupler, Narda, San Diego, CA, United States). A power meter (R&S NRP2 Power Meter, Rohde & Schwarz, Columbia, MD, United States) was connected to the other port on the directional coupler to measure the radiation. Both the forward power and reflected power can be measured by switching the position of antenna and signal generator on the directional coupler. The return loss, S11, of the antenna was calculated from the difference between the reflected power and the forward power. By sweeping the power frequency of the signal generator, the relationship between S11 and frequency was established. CST Studio Suite was used to simulate the return loss S11 and 3D far-field radiation pattern of the printed origami antenna. The relative permittivity,  $\varepsilon_r$  and dissipation factor,  $\tan \delta$ , were set as 6.89 and 0.613, respectively.

#### 3. Results

# 3.1 The process-microstructure relationships for Li<sub>2</sub>MoO<sub>4</sub>

# 3.1.1 Effect of compaction pressure on particle fusion

To study the effect of compaction pressure on the microstructure of Li<sub>2</sub>MoO<sub>4</sub> in HJF, the ink saturation level (or ink weight concentration) was fixed at 15 wt.%, and multiple specimens were fabricated with different compaction pressures from 1 MPa to 50 MPa. The SEM images in Fig.3a, a1 show the morphology of the raw Li<sub>2</sub>MoO<sub>4</sub> powder after sieving. The SEM images in Fig.3b-d show the fractured surfaces of the specimens. The results suggest that as the pressure increased from 1 MPa to 50 MPa, the interparticle pores (indicated by the yellow arrows) decreased significantly in size. Furthermore, the enlarged SEM images in Fig.3b1-d show that as the compaction pressure increased, the grain size decreased, and the grain boundary area became larger (indicated by the red diamond arrows).

# 3.1.2 Effect of ink saturation level on particle fusion

To study the effect of ink saturation level on the microstructure of Li<sub>2</sub>MoO<sub>4</sub>, specimens were fabricated with an ink saturation level varying from 0 wt.% to 15 wt.%. The compaction pressure was kept the same at 1 MPa. The SEM images in Fig.3e-h show the fractured surfaces of the fabricated specimens. The results indicate that the porosity decreased as the ink saturation level increased from 5 wt.% to 15 wt.%. This is likely because a greater amount of the particle surface was dissolved in the water when a higher saturation level was achieved, and hence more precipitates were formed between the particles, resulting in a higher density and lower porosity.

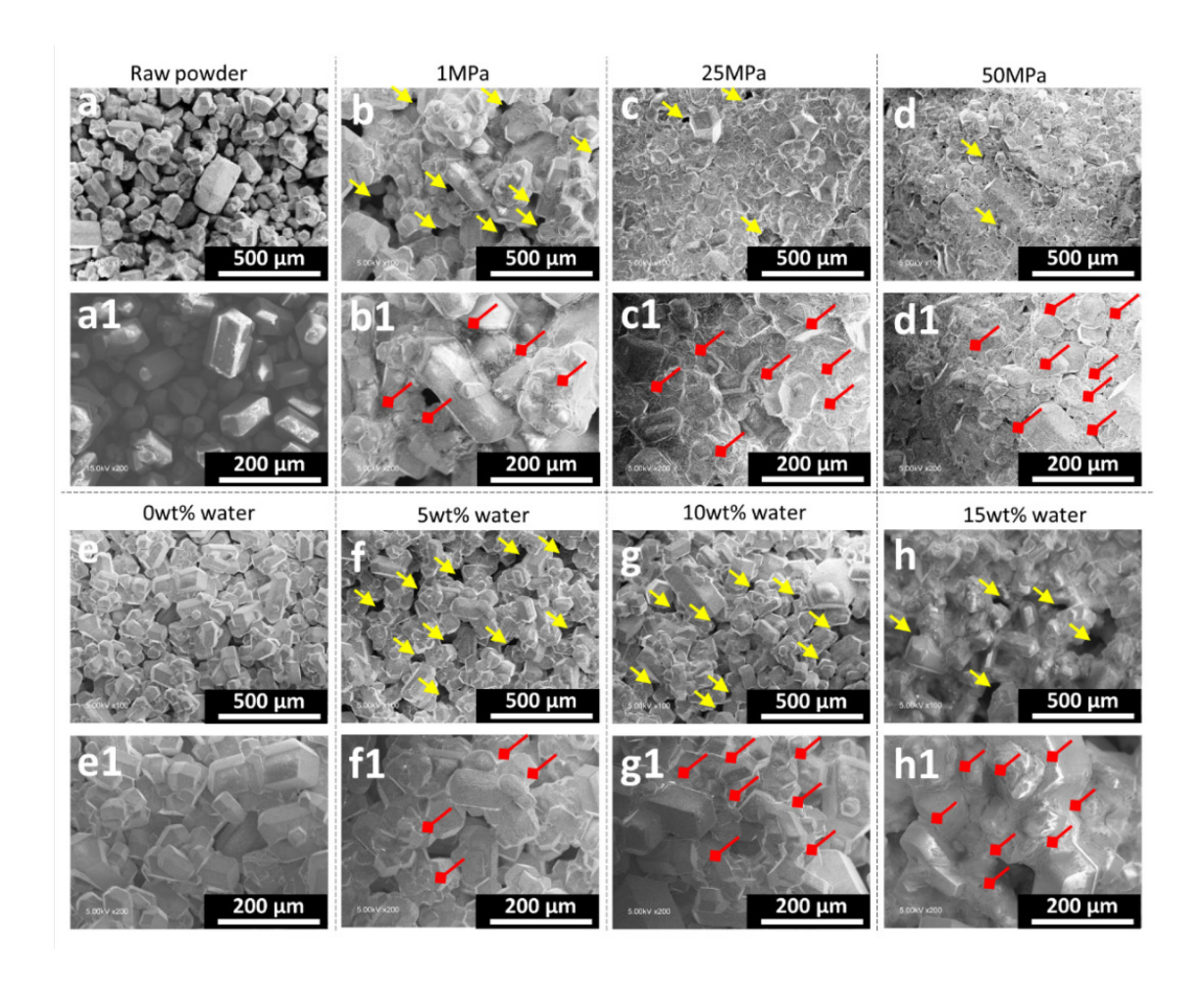


Fig.3 The SEM images of the fractured surfaces of the Li<sub>2</sub>MoO<sub>4</sub> specimens fabricated under different compaction pressures and ink saturation levels. a. The raw powder after sieving. The Li<sub>2</sub>MoO<sub>4</sub> specimen fabricated under 15 wt.% water and a pressure of b. 1 MPa, c. 25 MPa and d. 50 MPa. The Li<sub>2</sub>MoO<sub>4</sub> specimen fabricated under a compaction pressure of 1 MPa and an ink saturation level of e. 0 wt.%, f. 5 wt.%, g. 10 wt.% and h. 15 wt.%. a1-h1 are magnified SEM results corresponding to a-h. The yellow arrows mark the pore areas, and the red diamond arrows mark the bonding areas between grains.

# 3.1.3 Effect of ink chemistry on particle fusion

Different types of ink, including water and isopropyl alcohol, were utilized in fabrication to elucidate the role of water in particle fusion and densification in HJF. The fractured surfaces of the fabricated Li<sub>2</sub>MoO<sub>4</sub> specimens were observed using SEM (Fig.4a-d, a1-d1). Li<sub>2</sub>MoO<sub>4</sub> powder exhibits slight solubility in water but is insoluble in isopropyl alcohol. The compaction pressure was kept the same (1 MPa or 50

MPa). At a compaction pressure of 1 MPa, the grains in the specimens (Fig.4b, d) did not change significantly compared to the particle size of the raw powder (Fig.4a). The grains in the specimen fabricated with alcohol (Fig.4b, b1) had a sharp-edged morphology similar to the particle shape of the raw powder (Fig.4a, a1). In contrast, the grains in the specimen fabricated with water (Fig.4c, 3d) exhibited rounded edges, likely due to dissolution of the particles at the contact points. Under a high compaction pressure of 50 MPa, the grains in the specimen fabricated with alcohol (Fig.4f, f1) displayed a similar fractured morphology as that in the dry powder (Fig.4e, e1), while the grains in the specimen fabricated with water (Fig.4h, h1) underwent critical size reduction due to the combined effects of particle fracture and ink dissolution, resulting in a significant reduction in porosity. These findings suggest that the solubility of the particles in the ink is the dominant factor affecting the particle fusion and densification.

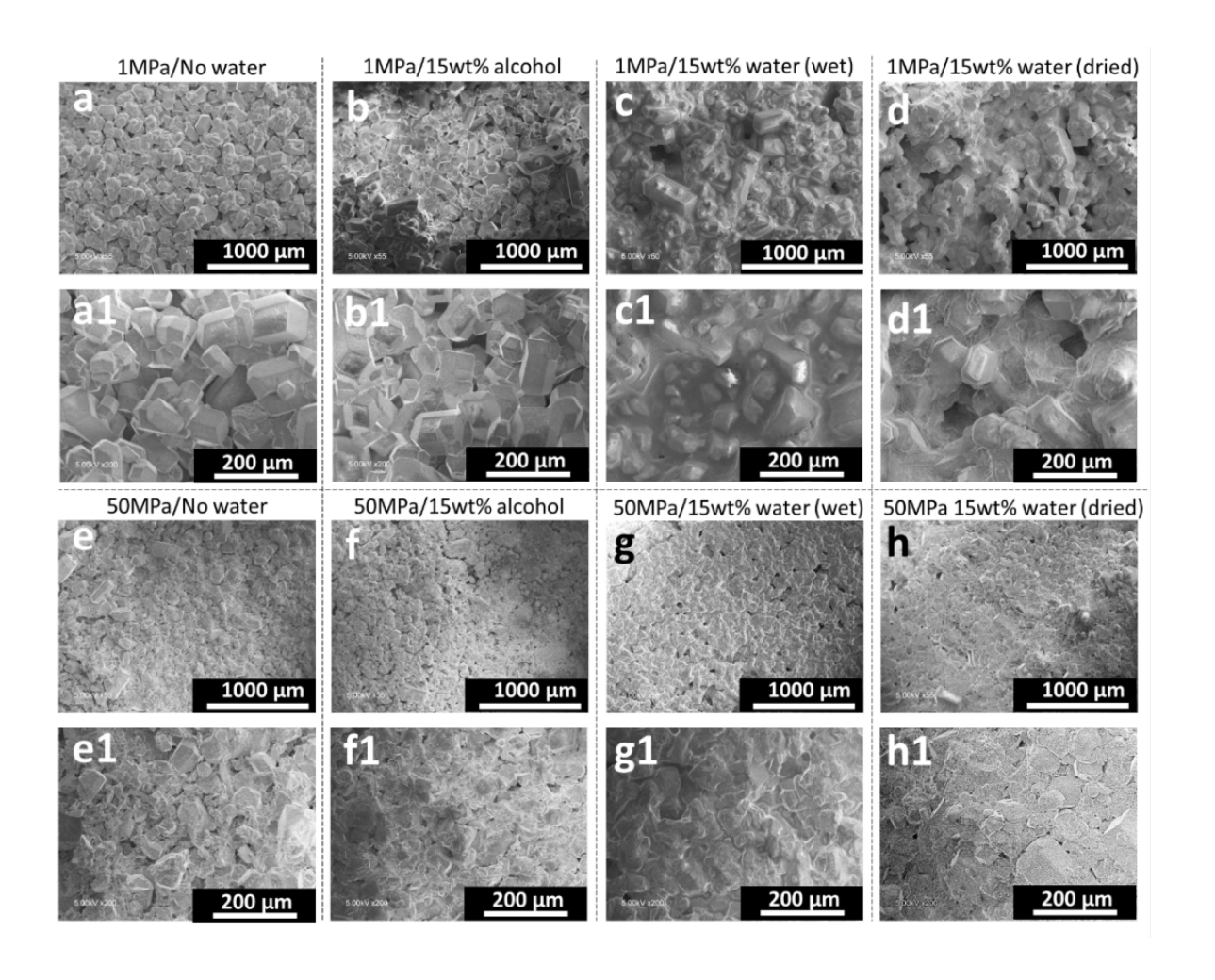


Fig.4 SEM images of a Li<sub>2</sub>MoO<sub>4</sub> specimen fabricated under a compaction pressure of 1 MPa and a. 0 wt.% water, b. 15 wt.% alcohol (dried), c. 15 wt.% water (wet) and d. 15 wt.% water (dried). SEM images of a Li<sub>2</sub>MoO<sub>4</sub> specimen fabricated under a compaction pressure of 50 MPa and e. 0 wt.% water, f. 15 wt.% alcohol (dried), g. 15 wt.% water (wet) and h. 15 wt.% water (dried). a1-h1 are magnified SEM results corresponding to a-h.

# 3.2 The process-property relationships for Li<sub>2</sub>MoO<sub>4</sub>

## 3.2.1 Density

The effects of compaction pressure and ink saturation level on the density of fabricated Li<sub>2</sub>MoO<sub>4</sub> specimens are illustrated in Fig.5a. The results indicate that, when the ink saturation level was 0 wt.% (i.e., no water), the relative density of the specimen increased from 57.07% to 72.58% as the compaction pressure increased. When the ink saturation level was 5wt.%, the density increased from 64.89% to 83.60% as the pressure increased. Under the same compaction pressure, the density of the specimen fabricated with an ink saturation level of 5 wt% was always higher than that of the dry specimen (0 wt.% ink saturation level), and their disparity became greater as the pressure level increased. This increase suggests the critical role of water in fusing ceramic particles during the HJF process. When the ink saturation level further increased from 5 wt.% to 15 wt.%, the densities did not change obviously since the excess amount of the liquid was squeezed out of the particle during the compaction and did not contribute to the particle fusion.

Fig. 5b shows the relationship between the number of compaction cycles and density. When the compaction pressure was equal to or greater than 150 MPa, the density increased by 5% as the number of compaction cycles increased from 1 to 5 but decreased as the number of compaction cycles increased to 10. In contrast, when the compaction pressure was equal to or less than 100 MPa, similar densities were achieved regardless of the number of compaction cycles. These results suggests that a certain number of compaction cycles under high pressures (>100 MPa) enhance the density of Li<sub>2</sub>MoO<sub>4</sub> in the HJF process, but applying too may cycles (>10) may reduce density due to water evaporation and damage to the

samples. On the other hand, the number of compaction cycles under low pressures (<100 MPa) has little influence on density likely because it takes less time to reach such pressure levels with minimal water evaporation.

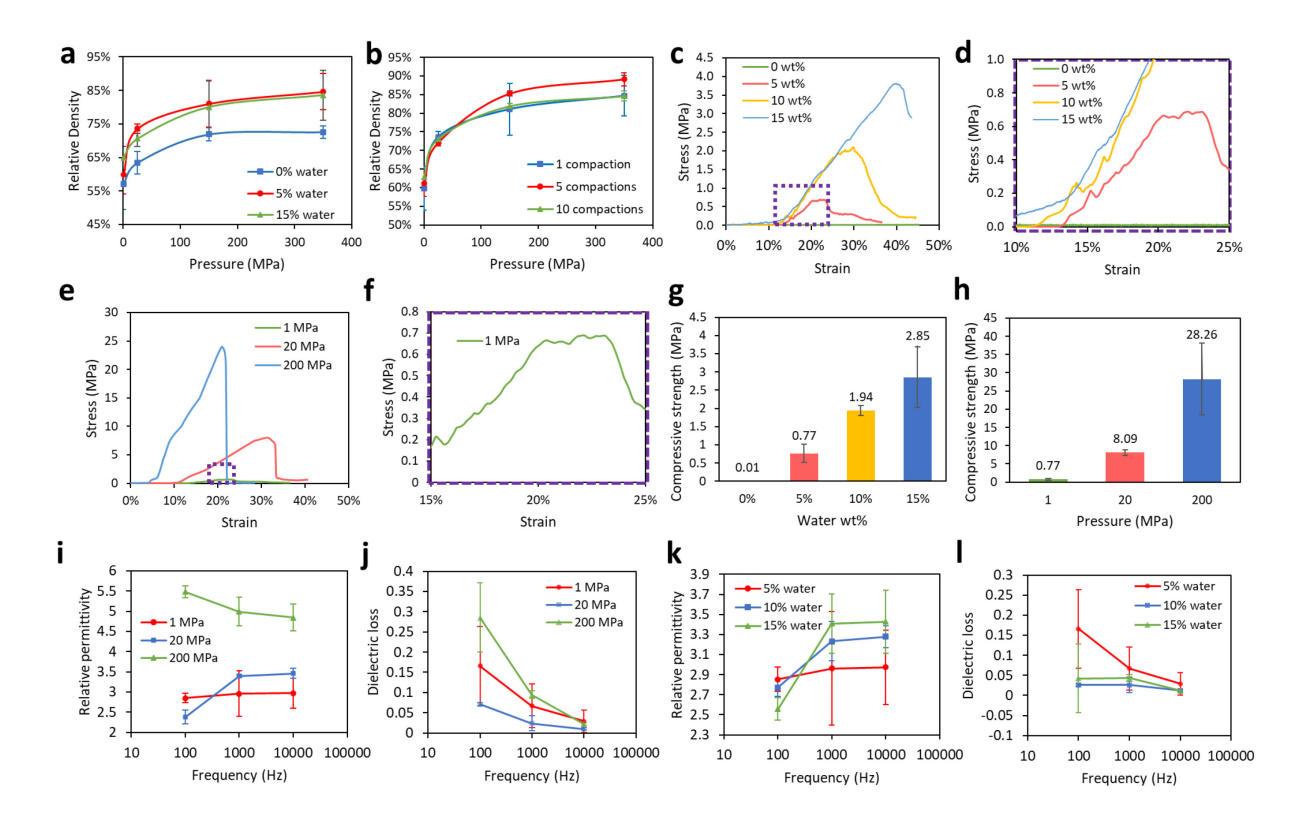


Fig.5 The process-property relationships for fabricated Li<sub>2</sub>MoO<sub>4</sub> ceramics. The relationship between relative density and compaction pressure: a. under different ink saturation levels and b. numbers of compaction cycles. c. Compression testing results of specimens fabricated under different ink saturation levels. d. Zoom-in results of compression test in a strain range of 10% to 25%. e. Compression testing results under different compaction pressure levels. f. Zoom-in results of compression test in a strain range of 15% to 25%. Compressive strengths of specimens fabricated under g. different ink saturation levels and h. compaction pressure levels. i. Frequency-dependent relative permittivity of specimens fabricated under different compaction pressure levels. The ink saturation level was fixed at 5 wt.%. j. Frequency-dependent dielectric loss of specimens fabricated under different compaction pressures. The ink saturation level was fixed at 5 wt.%. k. Frequency-dependent relative permittivity of specimens fabricated under

different ink saturation levels. The compaction pressure was fixed at 1 MPa. 1. Frequency-dependent dielectric loss of specimens fabricated under different ink saturation levels. The compaction pressure was fixed at 1 MPa.

# 3.2.2 Compressive strength

The compression testing results of Li<sub>2</sub>MoO<sub>4</sub> specimens fabricated under various ink saturation levels (0, 5 wt.%, 10 wt.% and 15 wt.% water) are illustrated in Fig.5c, d. The compaction pressure was kept constant at 1 MPa. The compressive strength of the specimens showed an increasing trend from 0.01 MPa to 2.85 MPa when the ink saturation level was raised from 0 wt.% to 15 wt.% (Fig.5g) because of enhanced bonding conditions between the particles, which matches the microstructures in Fig.3e-h. The compressive strength under an ink saturation level of 0 wt.% was close to zero, indicating that the Li<sub>2</sub>MoO<sub>4</sub> particles cannot be bonded together by an applied compaction pressure without the presence of water. This provides direct evidence for the essential effect of water on particle fusion in the HJF process. In the specimen fabricated under an ink saturation level of 5 wt.%, a stress peak of 0.21 MPa was first observed at a strain of 14.7% (Fig.5d), which may result from minor defects (such as crack or voids) introduced during the fabrication process. The specimen did not completely fail until the strain reached 22.1%. The compression testing results of specimens fabricated under three different compaction pressures (1, 50 and 150 MPa) are shown in Fig.5e, f. The ink saturation level was kept the same at 5 wt.%. Fig.5h illustrates that the specimens fabricated under higher compaction pressure attained higher compressive strength due to their smaller grain size and reduced porosity, as shown in Fig.3b-d. These results suggest that compaction pressure acts as a key driving force for particle fusion and densification in HJF.

# 3.2.3 Dielectric properties

Ceramics with low relative permittivity and low dielectric loss are beneficial to high-frequency applications [52, 53]. Fig.5 i-l illustrate the effects of compaction pressure and ink saturation level on the dielectric properties of fabricated Li<sub>2</sub>MoO<sub>4</sub> specimens. The results in Fig.5 i and k show that at high

frequencies (equal to or greater than 1000 Hz), the relative permittivity increased with increasing compaction pressure or ink saturation level. At a relatively lower frequency (e.g., 100 Hz), the relatively permittivity did not show significant changes with the ink saturation level, but it decreased slightly by 16% as the compaction pressure increased from 1 MPa to 20 MPa and increased significantly as the pressure continued to increase to 200 MPa.

Fig. 5 j and 1 illustrate that the dielectric loss decreased to be less than 0.05 as the frequency increased from 100 to 10000 Hz, due to the reduction of space charge polarization effect [54]. In Fig. 5 j, when the compaction pressure is lower than 20 MPa, increasing the compaction pressure resulted in smaller dielectric loss, largely due to enhanced density in the samples. However, the dielectric loss increased again when the compaction pressure further increased to 200 MPa, which was likely caused by internal defects introduced by the high pressure. Meanwhile, in Fig. 5 l, the dielectric loss decreased monotonically as the ink saturation level increased from 5% to 15%.

In summary, the HJF process can achieve low relative permittivity and dielectric loss simultaneously at high frequency (10000 Hz) by using relatively low compaction pressure (e.g., 1 MPa) and low ink saturation level (e.g., 5%). Moreover, the dielectric properties of printed samples can be locally tuned by selectively applying different compaction pressures and ink saturation levels in the future development of the HJF process.

## 3.3 Numerical modeling of the mass transfer between particles in the HJF process

The mass transfer between particles in HJF is governed by a dissolution-diffusion-precipitation process (Fig.6a, a1, a2). Under the compaction pressure, ceramic particles come into contact with each other, and a contact stress is induced at the contact point between the particles, which accelerates the dissolution of the particle surface into the volatile dissolving ink in the interparticle pore (red arrows in Fig.6a1), as shown in the following reaction formula [55]:

$$Li_2MoO_4(s) \xrightarrow{H_2O} 2Li^+(aq) + MoO_4^{2-}(aq)$$
 (1)

Due to a concentration gradient of solutes in the ink, the dissolved species (dark grey color in Fig.6a1) diffuse from the interparticle contact point into the pore (dark blue arrows in Fig.6a1). Meanwhile, micro cracks may form at the contact point (as shown in Fig.6a2) as a result of subcritical crack growth [56], which leads to a greater surface area of the particles being exposed to the link. The interaction between the ink and the micro cracks subsequently accelerates the dissolution of the particles near the crack tips, causing more materials from the particles to diffuse into the interparticle pore.

In the last step of the HJF process when a mild heating temperature is applied to the powder bed, the ink in the pore is evaporated, while the dissolved material precipitates at the neck region, leading to the bonding of the two particles in contact. The precipitation process follows the chemical reaction:

$$2Li^{+}(aq) + MoO_4^{2-}(aq) \xrightarrow{\Delta} Li_2MoO_4(s)$$
 (2)

A multi-phase multi-physics model was developed to explain the particle fusion mechanisms described above. A four-particles system was used in the simulation, as illustrated in Fig.6b. The pore region (white color) between the four particles represents the fluid phase. A solid-fluid interface was defined at the boundary between the solid and fluid phases surrounded by the yellow dashed curves in Fig.6b. A compaction pressure was applied on the top boundary of the model. As a result, the distribution of stress can be calculated in the solid phase of particle system, as shown in Fig.6c. The surface reactions (i.e., surface dissolution, fracture-induced dissolution, precipitation) between the particles and the ink were modelled by a first-order kinetics model [57]. Fig.6e depicts the dissolution velocity calculated on the particles' surface. The complex dynamics of the solid-liquid interface resulting from the surface reaction was captured using a level set method [58, 59]. Fig.6d illustrates the initial condition of the model's level set function, where a level set value smaller than 0 represents solid phase in the model, and a level set value larger than 0 represents liquid phase. The regions whose level set value equals zero define the boundary between the solid and liquid phases. The governing equations of the proposed model are described in Supplementary Section 1.

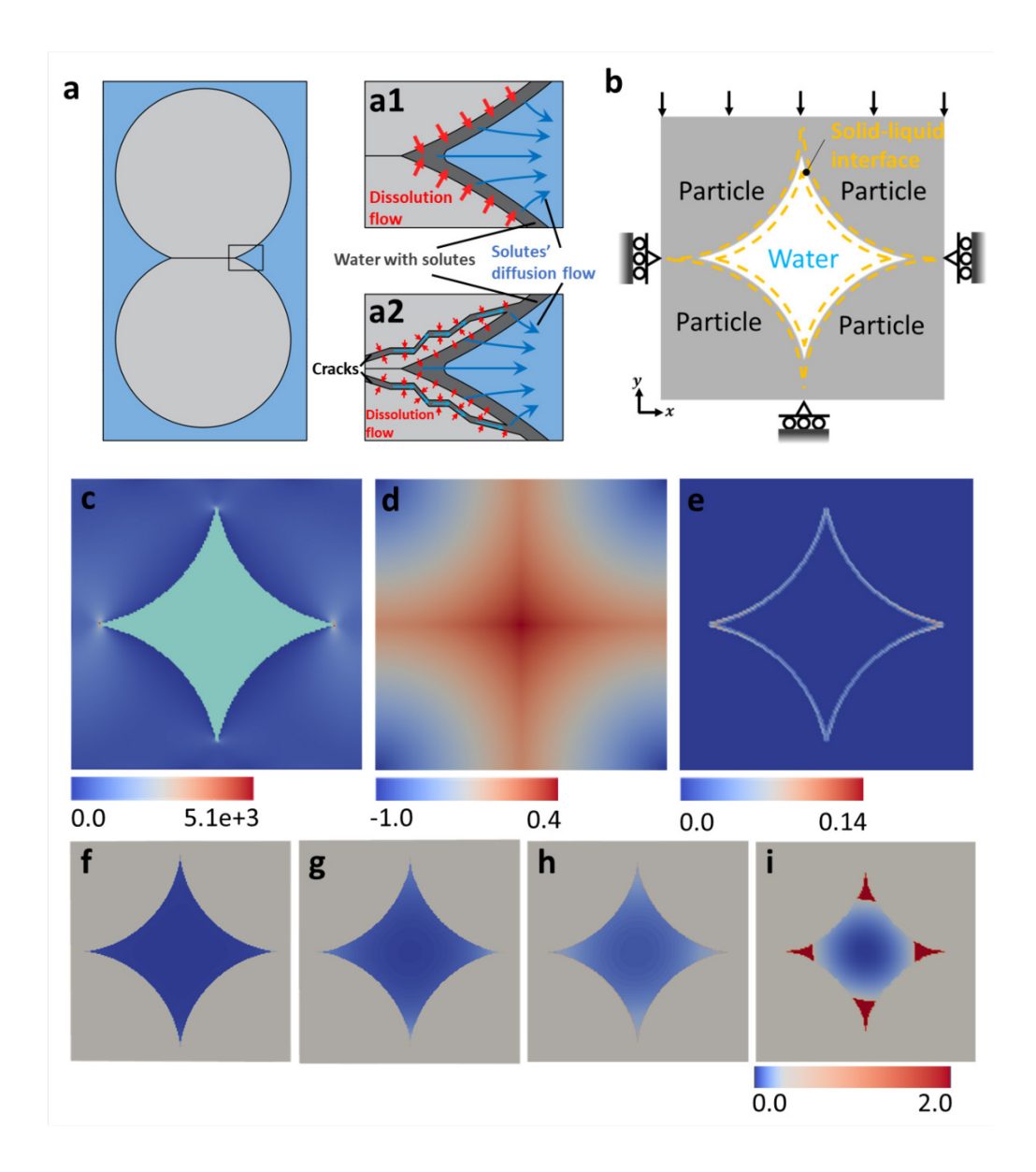


Fig.6 Numerical modeling of the particle fusion mechanism in HJF. a. Schematic of mass transfer between particles: a1. Surface dissolution of particles; a2. Fracture-induced dissolution of particles. b. Phases and boundary conditions of the numerical model for mass transfer between particles. c. Stress distribution in the solid phase when a compaction pressure of 1 MPa was applied. d. Level-set function along the simulation space when t=0. e. Interface velocity in the solid-liquid interface when t=0. Particle boundaries in the solid phase (grey color region) and relative concentration of dissolved ceramic nanoparticles in the liquid phase (blue region in the center) during dissolution when t=0, t=0.25

second and h. t = 0.5 second. i. Precipitation result after the liquid phase is evaporated. Solutes in the liquid phase precipitate when their relative concentration reached 1.

Fig. 6f-i displays the simulation results of the particle fusion mechanism in the HJF process. Fig. 6f depicts the particles' initial status at t = 0 s when the concentration of the solutes in the liquid phase was zero. After a compaction force was applied, the particle surfaces started to dissolve in the liquid, and the centers of the particles got closer to each other (Fig. 6g, t = 0.25 s). Due to a higher stress induced at the contact points between the particles, the solute concentration near the neck regions was higher than in the other regions, leading to the dissolved material diffusing towards the center of the interparticle pore. As the dissolution-diffusion process continued, the solute concentration in the center of the pore increased (Fig. 6h, t = 0.5 s). After that, the compaction pressure was removed, and a heating temperature of 100 °C was applied to the system to evaporate the liquid. As the solute concentration in the liquid phase reached equilibrium, the dissolved solid precipitated in the areas near the neck regions (Fig. 6i). The location of the precipitates in the simulation results illustrates how loose particles are bonded together in the HJF process, which match the morphology of particle fusion (red diamond arrows in Fig. 3b2, h1).

#### 3.4 Test cases

#### 3.4.1 Complex 3D structures

Fig. 7 shows test cases with complex 3D geometries, including gear, hollow ring, Möbius ring, shaft support, lattice structure, Iowa Hawkeye, oil & gas mud pump, and bevel gear. A compaction pressure of 1 MPa was selected for the fabrication to achieve the optimal printing fidelity in our current printing system [60]. The optimized jetting parameters (e.g., stroke, nozzle size) were identified to control the ink saturation level in the powder bed (see Supplementary Section 2). A layer thickness of 0.4 mm was selected to ensure the full penetration of a deposited droplet through a layer.

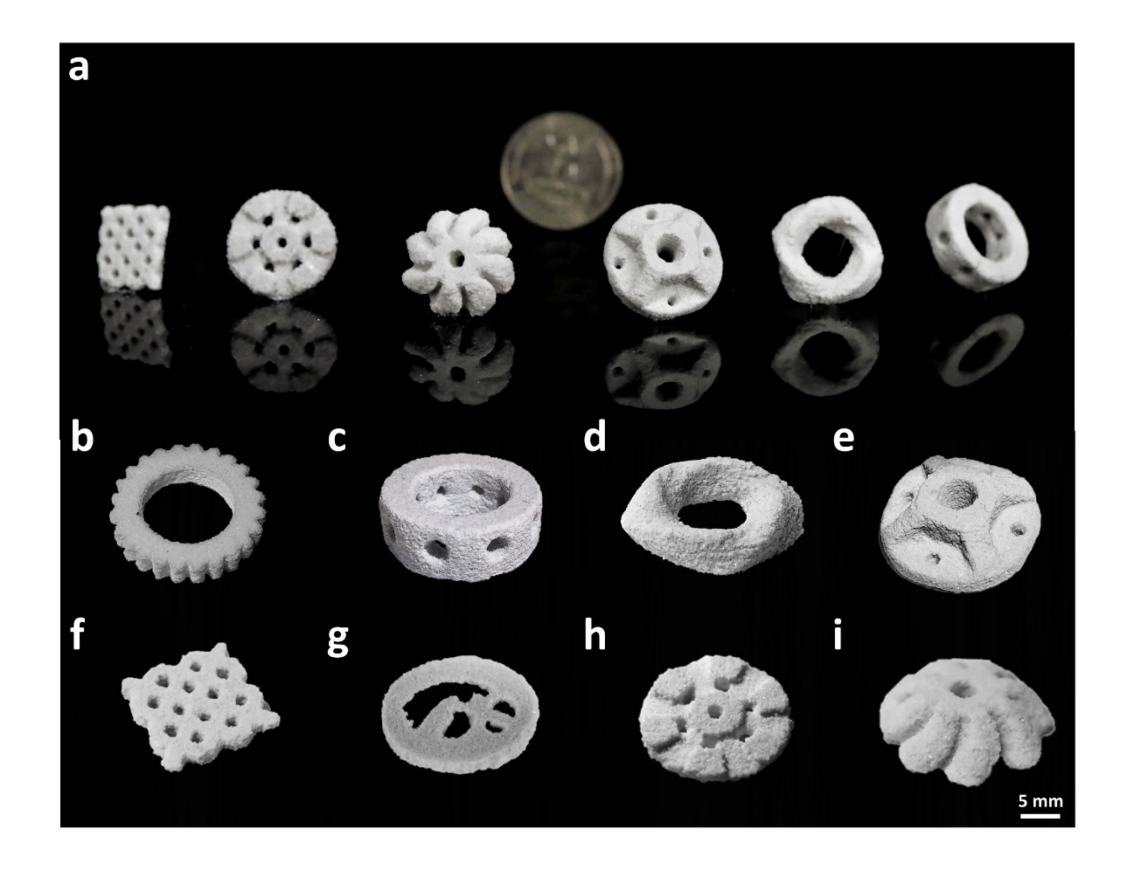


Fig. 7 Fabrication results of the HJF process. a. 3D-printed samples fabricated via the HJF process. b. Gear. c. Hollow ring. d. Möbius ring. e. Shaft support. f. Lattice structure. g. Iowa Hawkeye. h. Oil & Gas Mud Pump. i. Bevel gear.

#### 3.4.2 Patch antennas

To demonstrate the capability of HJF in co-printing ceramics with other dissimilar materials (metals and polymers), two types of Li<sub>2</sub>MoO<sub>4</sub> patch antennas were fabricated using the HJF process, including a circular patch antenna and an origami patch antenna (refer to Fig.8). As a low-K (permittivity) dielectric material, Li<sub>2</sub>MoO<sub>4</sub> can be integrated with different electronic and structural materials to form multifunctional patch antennas for various high-frequency applications [61]. A patch antenna contains four layers, including a metal-based conductive patch layer (top layer), a ceramic-based dielectric substrate (middle layer), a metal-based conductive ground layer (bottom layer), and a nylon-based protection layer. The top and bottom layers were made from copper foil sheets, and the middle layer was fabricated from

Li<sub>2</sub>MoO<sub>4</sub>. The fabrication process of the patch antennas is illustrated in Fig.8a-d: The digital design of a dielectric substrate was first generated for the antenna using a computer-aided design (CAD) software (Fig.8a, a1); the digital design was then printed with the Li<sub>2</sub>MoO<sub>4</sub> powder via the HJF process (Fig.8b, b1); afterwards, a copper patch layer was embedded into the powder bed (Fig.8c, c1); finally, a nylon layer was printed on top of the copper patch layer as a protection layer (Fig.8d, d1). After the printing process was completed, another copper layer was attached to the other side of the Li<sub>2</sub>MoO<sub>4</sub> dielectric substrate as the ground.

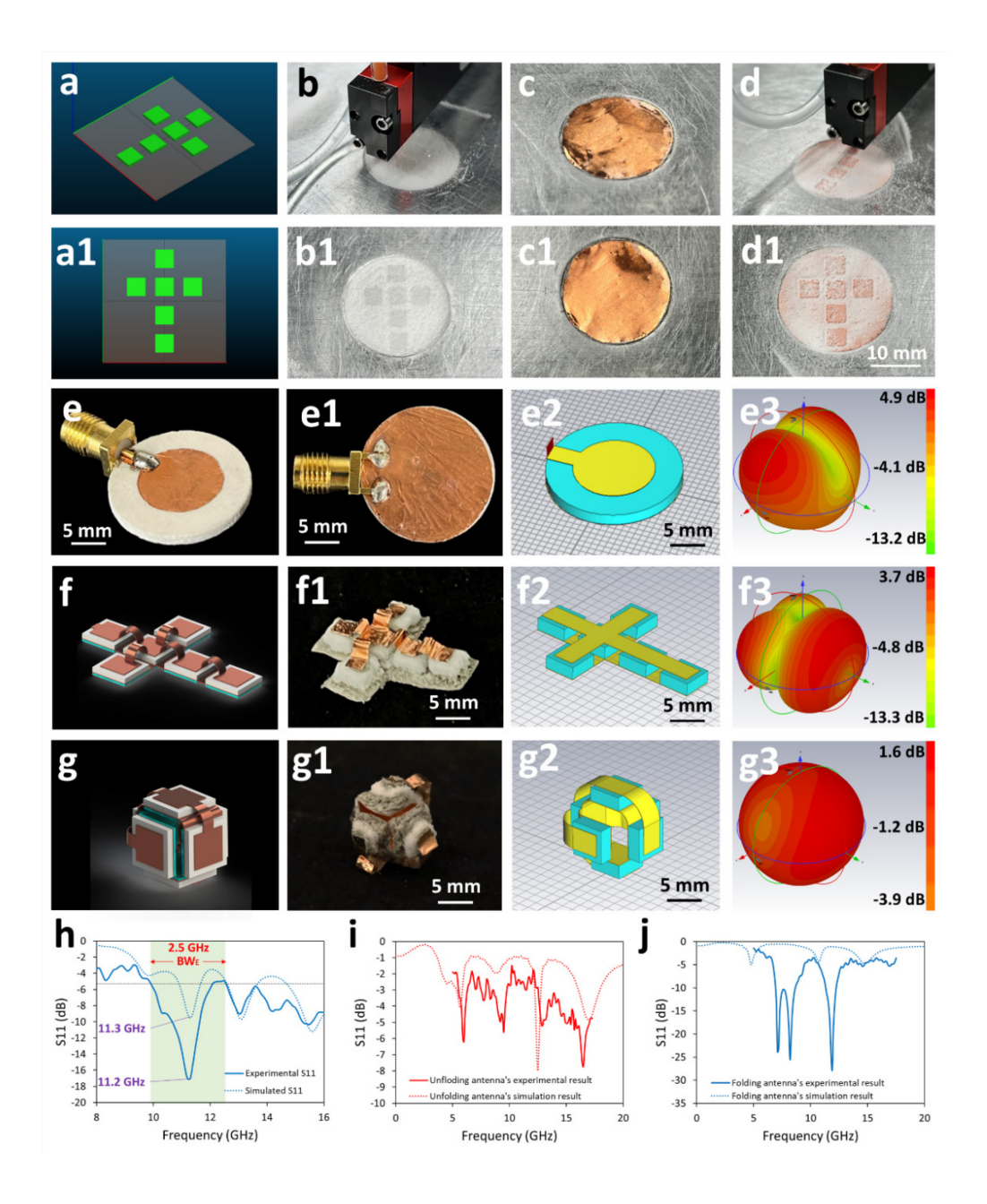


Fig. 8 Printing and characterization of patch antennas: a. oblique and a1. top views of the CAD model for Li<sub>2</sub>MoO<sub>4</sub> printing; b. oblique and b1. top views of the printing process for Li<sub>2</sub>MoO<sub>4</sub> components; c. oblique and c1. top views of the lamination process for a copper layer together with silver paste; d. oblique and d1. top view of the printing process for the nylon protection layer. e. Oblique and e1. bottom views of the circular patch antenna. e2. Design and e3. 3D far-field simulation of the circular patch antenna (frequency is 11.3 GHz). f. Design and f1. printing result of the unfolded origami antenna. f2.

Design and f3. 3D far-field simulation of the unfolded origami antenna (frequency is 10 GHz). g. Design and g1. printing result of the folded origami antenna. g2. Design and g3. 3D far-field simulation of the folded origami antenna (frequency is 10 GHz). Comparisons of the experiment and simulation results of reflection loss S11 for h. the circular patch antenna, i. the unfolded origami antenna and j. the folded origami antenna.

The top and bottom views of the circular patch antenna are shown in Fig.8e, e1. The top patch layer has a circular shape with a diameter of 12 mm, and both the bottom ground layer and the Li<sub>2</sub>MoO<sub>4</sub> substrate have a diameter of 20 mm. The thickness of the Li<sub>2</sub>MoO<sub>4</sub> substrate is 2 mm. A SMA port was soldered to the top and bottom layers of the circular antenna to measure its performance. The 3D far-field plot of the circular patch antenna was simulated in CST Studio Suite (Fig.8e2, e3). The measured and simulated return loss, S11, of the fabricated circular patch antenna are shown in Fig.8h. The simulated and experimental resonant frequencies of the antenna are 11.3 GHz and 11.2 GHz, respectively, which are in the X-band region and suitable for applications of wireless computer networks, radar, and satellite communication. The experimental and simulated values of S11 at the resonant frequencies are found to be -17.03 dB and -9.50 dB, accordingly. The bandwidth of the experimental results, BW<sub>E</sub>, is defined as the frequency range where the S11 value is less than -5 dB. Based on that, BW<sub>E</sub> of the circular patch antenna is 2.5 GHz, as depicted in Fig.8h. The difference between the experimental and simulated results (i.e., resonant frequency, return loss and bandwidth) can be attributed to the solder joint of the SMA port to the antenna's top and bottom layers, the air gap between the dielectric substrate and the top/bottom layer, and/or the low-frequency dielectric properties used in the simulation.

The design and fabrication results of an origami antenna under the unfolded state are shown in Fig.8f, f1. The origami antenna can be reconfigured from the unfolded state into a cubic geometry (Fig.8g, g1). The simulated 3D far-field plots of the origami antenna under the unfolded and folded states at 10 GHz are shown in Fig.8f3, g3, respectively. The unfolded antenna features a directional radiation pattern with a fluctuation from the maximum directivity to the minimum of 17 dB; the radiation pattern of the folded

state is nearly isotropic, with a fluctuation from the maximum directivity to the minimum of 5.4 dB. The return losses S11 of the unfolded and folded origami antennas under a frequency between 5 GHz and 18 GHz were measured and simulated, as depicted in Fig.8i, j, respectively. Multiple S11 peaks could be observed for both the unfolded and folded states, where the unfolded one had four experimental resonant frequencies at 6 GHz, 9.5 GHz, 12.6 GHz and 16.5 GHz, and the folded antenna had three experimental resonant frequencies 7.1 GHz, 8.2 GHz and 11.9 GHz. The maximum return losses S11 of the unfolded and folded states were -7.74 dB at 16.5 GHz, and -27.76 dB at 11.9 GHz, respectively. The simulated return losses (dashed curves in Fig.8Error! Reference source not found.i, j) successfully predicted the number of resonant frequencies for the unfolded and folded states, but manifested relatively low return loss values compared to the experimental results (solid curves in Fig.8i, j), which is due to the solder joint and air gap issues mentioned above. The difference in the maximum return losses and resonant frequencies between the folded and unfolded states indicates that the design and fabrication of origami antennas using the HJF process are beneficial to tuning the antennas' properties and performance. It also highlights the capability of the HJF process to achieve multi-material printing for ceramic-based composite materials and electronic applications.

#### 4. Discussion

# 4.1 Materials applicable for HJF

Li<sub>2</sub>MoO<sub>4</sub> is not the only material that can be applied for the HJF process. Table 1 shows some other ceramic materials that are considered suitable for the HJF process [49]. For ceramic materials with high solubility in water, such as V<sub>2</sub>O<sub>5</sub> and Li<sub>2</sub>MoO<sub>4</sub>, pure DI water can be selected as the volatile dissolving ink. For ceramic materials with limited or incongruent solubility in water, such as BaTiO<sub>3</sub>, an aqueous suspension of its precursor nanoparticles (i.e., Ba(OH)<sub>2</sub> and TiO<sub>2</sub>) can be used as the ink, where the Ba<sup>+</sup> source in the suspension inhibits the dissolution of Ba<sup>+</sup> from the surface area of BaTiO<sub>3</sub> particles and reacts with the Ti source in the suspension to form BaTiO<sub>3</sub> precipitates through a hydrothermal reaction [50, 51]:

$TiO_2 + Ba(OH)_2 = BaTiO_3 + H_2O$	(3)	)
-------------------------------------	-----	---

Table 1 Ceramic materials that are suitable for the HJF process.

Binary Type	Ternary Type	Quaternary Type
$V_2O_5$	Li <sub>2</sub> MoO <sub>4</sub>	LiFePO <sub>4</sub>
ZnO	Li <sub>2</sub> CO <sub>3</sub>	LiCoPO <sub>4</sub>
MgO	BaTiO <sub>3</sub>	KH2PO <sub>4</sub>
$ZrO_2$	ZnMoO <sub>4</sub>	Ca <sub>5</sub> (PO <sub>4</sub> ) <sub>3</sub> (OH)

# 4.2 Comparison with other AM processes for ceramics

BJ and powder bed fusion (PBF) are two other powder-bed-based AM processes for ceramics (refer to ISO/ASTM 52900:2021), similar to our HJF process. All three processes require a certain particle size (e.g., >10 μm) for the feedstock powder to maintain flowability during printing [62]. However, there are several differences between these processes in terms of binder materials used, printing temperatures, and green density achieved. A comparison between these AM processes is listed in Table 2.

Table 2 Comparison between HJF, BJ and direct laser PBF processes

AM Processes	Binder materials used	Printing temperature	Green density achieved
HJF	Inorganic binder	Moderate (80-160 °C)	Up to 90%
BJ	Organic binder	Moderate (~200 °C)	Up to 67%
Direct PBF	No binder needed	High (>400 °C)	NA

- (1) Binder materials used. As discussed in Section 4.1, the HJF process only requires inorganic binders, such as DI water or certain inorganic suspensions, to form the green. In contrast, the BJ process uses organic binders composed of vinyl, acrylic, and cellulose [5, 63] to bond particles. These binders are either deposited via a printhead or premixed in the powder bed [65]. The PBF process, especially direct laser PBF, does not utilize any binders but instead directly melts or sinters the ceramic powder with a laser.
- (2) Printing temperatures. Both the HJF and BJ processes use relatively low temperatures during fabrication. The HJF process requires a mild temperature between 80 °C and 160 °C [22, 60, 66, 67] to fuse the ceramic particles together, while the BJ process relies on a moderate temperature (180-200 °C) to cure the organic binder and strengthen the green part [20, 65, 68]. In addition, BJ requires

a debinding step (600 °C) and a sintering step (over 1000 °C) to purify and densify the green parts, while the HJF process eliminates the need for debinding and requires only an optional sintering step with a reduced sintering temperature to further densify the parts. Direct laser PBF process, on the other hand, requires a high temperature above 400 °C to preheat the powder bed and reduce keyhole formation in the printed results. The melting/sintering temperature in direct laser PBF can reach up to 1600 °C [18, 69, 70].

(3) Green density achieved. The HJF process is capable of achieving a high green density, up to 90%, as shown in Fig.5a. In contrast, the BJ process achieves a much lower green density (e.g., ~67% [71]) partially due to the usage of organic binders. Direct laser PBF can potentially achieve an extremely high density by completely melting the ceramic powder, but this process is prone to thermal shock cracking, which remains a significant challenge [18].

Overall, the HJF process offers a unique advantage among ceramic AM processes due to its ability to achieve high green density as well as binder-free, low-temperature fabrication using a water-based ink and hydrothermal fusion mechanism.

## 5. Conclusions

In this paper, a binder-free additive manufacturing method named hydrothermal-assisted jet fusion is proposed. Inspired by the lithification process in nature, HJF is capable of printing complex ceramic structures without the need for organic binders which are typically required in most existing ceramic AM processes. The particle fusion in the HJF process is governed by a hydrothermal-mediated dissolution-diffusion-precipitation process. To better understand the effects of different process parameters (e.g., compaction pressure, ink saturation level, compaction time) on the mass transfer in the HJF process, the microstructures and macroscopic properties of HJF-printed specimens (i.e., Li<sub>2</sub>MoO<sub>4</sub>) were studied. For Li<sub>2</sub>MoO<sub>4</sub>, a higher compaction pressure, a greater ink saturation level, or a longer compaction time can enhance the density and compressive strength of HJF-printed parts. The relative permittivity of printed specimens increased with an increasing compaction pressure and ink saturation level, while the dielectric

loss initially decreased and then increased with the increase in compaction pressure but decreased with an increase in ink saturation level. To validate the fusion mechanism in the HJF process, a multi-phase multi-physics numerical model was established. The simulation results indicate that the dissolution-diffusion-precipitation process leads to the formation of bonding neck between the particles, which matches our experimental observations. Ceramic complex 3D structures and patch antennas were printed using the HJF process, indicating the capability of the HJF process in building geometrically and compositionally complex materials.

# 6. Acknowledgement

This work is, in part, supported by the US National Science Foundation under grant number CMMI-2236905. The authors would like to thank Philip Thompson for his kind support on antenna's return loss measurement and the donation of the equipment from Skyworks Solution, Cedar Rapids Design Center and Qorvo Design Center in Hiawatha, Iowa. The authors would also like to thank Dr. David R. Andersen for the helpful suggestions regarding the radiation pattern results.

## References

- 1. Gonzalez-Gutierrez, J., et al., Additive manufacturing of metallic and ceramic components by the material extrusion of highly-filled polymers: A review and future perspectives. Materials, 2018. **11**(5): p. 840.
- 2. Griffith, M.L. and J.W. Halloran, *Freeform fabrication of ceramics via stereolithography*. Journal of the American Ceramic Society, 1996. **79**(10): p. 2601-2608.
- 3. Bártolo, P.J., *Stereolithography: materials, processes and applications*. 2011: Springer Science & Business Media.
- 4. He, L., et al., Support-free ceramic stereolithography of complex overhanging structures based on an elasto-viscoplastic suspension feedstock. ACS applied materials & interfaces, 2019. **11**(20): p. 18849-18857.
- 5. Lv, X., et al., Binder jetting of ceramics: Powders, binders, printing parameters, equipment, and post-treatment. Ceramics International, 2019. **45**(10): p. 12609-12624.
- 6. Du, W., et al. *Binder jetting additive manufacturing of ceramics: A literature review*. in *ASME International Mechanical Engineering Congress and Exposition*. 2017. American Society of Mechanical Engineers.
- 7. Lewis, J.A., *Direct-write assembly of ceramics from colloidal inks*. Current Opinion in Solid State and Materials Science, 2002. **6**(3): p. 245-250.

- 8. Lewis, J.A., et al., *Direct ink writing of three-dimensional ceramic structures*. Journal of the American Ceramic Society, 2006. **89**(12): p. 3599-3609.
- 9. Dermeik, B. and N. Travitzky, *Laminated Object Manufacturing of Ceramic-Based Materials*. Advanced Engineering Materials, 2020. **22**(9): p. 2000256.
- 10. Pekin, S., J. Bukowski, and A. Zangvil. *A Study on Weight Loss Rate Controlled Binder Removal From Parts Produced by FDC*. in 1998 International Solid Freeform Fabrication Symposium. 1998.
- 11. Lewis, J.A., *Binder removal from ceramics*. Annual Review of Materials Science, 1997. **27**(1): p. 147-173.
- 12. Stampfl, J., et al., *Rapid prototyping and manufacturing by gelcasting of metallic and ceramic slurries.* Materials Science and Engineering: A, 2002. **334**(1-2): p. 187-192.
- 13. Yang, H., et al., Fabrication of high performance ceramic microstructures from a polymeric precursor using soft lithography. Advanced Materials, 2001. **13**(1): p. 54-58.
- 14. Pham, T.A., et al., *Three-dimensional SiCN ceramic microstructures via nano-stereolithography of inorganic polymer photoresists.* Advanced Functional Materials, 2006. **16**(9): p. 1235-1241.
- 15. Felzmann, R., et al., *Lithography -based additive manufacturing of cellular ceramic structures*. Advanced Engineering Materials, 2012. **14**(12): p. 1052-1058.
- 16. Yang, L. and H. Miyanaji. *Ceramic additive manufacturing: a review of current status and challenges.* in *Solid Freeform Fabrication Symposium.* 2017.
- 17. Kruth, J.P., et al., *Binding mechanisms in selective laser sintering and selective laser melting.* Rapid prototyping journal, 2005.
- 18. Yves-Christian, H., et al., *Net shaped high performance oxide ceramic parts by selective laser melting.* Physics Procedia, 2010. **5**: p. 587-594.
- 19. Wilkes, J., et al., *Additive manufacturing of ZrO2 -Al2O3 ceramic components by selective laser melting.* Rapid Prototyping Journal, 2013.
- 20. Travitzky, N., et al., *Additive manufacturing of ceramic-based materials*. Advanced engineering materials, 2014. **16**(6): p. 729-754.
- 21. Monroe, J., *Physical Geology Exploring The Earth.* 2004.
- 22. Fei, F., et al., *Hydrothermal-Assisted Transient Binder Jetting of Ceramics for Achieving High Green Density.* JOM, 2020. **72**(3): p. 1307-1313.
- 23. Liu, Y., et al., *Development of the cold sintering process and its application in solid-state lithium batteries.* Journal of Power Sources, 2018. **393**: p. 193-203.
- 24. Berbano, S.S., et al., *Cold sintering process of Li1. 5Al0. 5Ge1. 5 (PO4) 3 solid electrolyte.* Journal of the American Ceramic Society, 2017. **100**(5): p. 2123-2135.
- 25. Seo, J.-H., et al., *Broad temperature dependence, high conductivity, and structure-property relations of cold sintering of LLZO-based composite electrolytes.* Journal of the European Ceramic Society, 2020. **40**(15): p. 6241-6248.
- 26. Leng, H., et al., *Cold sintering and ionic conductivities of Na3. 256Mg0. 128Zr1.* 872Si2PO12 solid electrolytes. Journal of Power Sources, 2018. **391**: p. 170-179.
- 27. Guo, J., et al., *Cold sintering process: a new era for ceramic packaging and microwave device development.* Journal of the American Ceramic Society, 2017. **100**(2): p. 669-677.

- 28. Wang, D., et al., *Cold sintering of microwave dielectric ceramics and devices*. Journal of Materials Research, 2021: p. 1-17.
- 29. Induja, I. and M. Sebastian, *Microwave dielectric properties of mineral sillimanite obtained by conventional and cold sintering process.* Journal of the European Ceramic Society, 2017. **37**(5): p. 2143-2147.
- 30. Liu, B., et al., Enhancement of densification and microwave dielectric properties in LiF ceramics via a cold sintering and post-annealing process. Journal of the European Ceramic Society, 2021. **41**(2): p. 1726-1729.
- 31. Wang, D., et al., *Cold sintering and electrical characterization of lead zirconate titanate piezoelectric ceramics*. APL Materials, 2018. **6**(1): p. 016101.
- 32. Huang, H., J. Tang, and J. Liu, *Preparation of NaO. 5BiO. 5TiO3 ceramics by hydrothermal-assisted cold sintering.* Ceramics International, 2019. **45**(6): p. 6753-6758.
- 33. Gupta, S., et al. *Cold Sintering of PZT 2-2 Composites for High Frequency Ultrasound Transducer Arrays*. in *Actuators*. 2021. Multidisciplinary Digital Publishing Institute.
- 34. Wang, D., et al., Fabrication of bimorph lead zirconate titanate thick films on metal substrates via the cold sintering-assisted process. Acta Materialia, 2020. **195**: p. 482-490.
- 35. Guo, H., et al., *Cold sintering process: a novel technique for low-temperature ceramic processing of ferroelectrics.* Journal of the American Ceramic Society, 2016. **99**(11): p. 3489-3507.
- 36. Ma, J., et al., *Composition, microstructure and electrical properties of KO. 5NaO. 5NbO3 ceramics fabricated by cold sintering assisted sintering.* Journal of the European Ceramic Society, 2019. **39**(4): p. 986-993.
- 37. Cong, L., et al., Effect of dwell time on cold sintering assisted sintering based highly transparent 0.9 KO. 5NaO. 5NbO3-0.1 LiBiO3 ceramics. Journal of Alloys and Compounds, 2020. **826**: p. 154249.
- 38. Costa, T., et al., *Infrared and thermogravimetric study of high pressure consolidation in alkoxide silica gel powders.* Journal of Non-Crystalline Solids, 1997. **220**(2-3): p. 195-201.
- 39. Tan, C. and H. Zhang, *Wet-chemical synthesis and applications of non-layer structured two-dimensional nanomaterials*. Nature communications, 2015. **6**(1): p. 1-13.
- 40. Nikam, A., B. Prasad, and A. Kulkarni, *Wet chemical synthesis of metal oxide nanoparticles: a review.* CrystEngComm, 2018. **20**(35): p. 5091-5107.
- 41. Kvist, A. and A. Lundén, *The Electrical Conductivity of Molten Lithium Molybdate*. Zeitschrift für Naturforschung A, 1965. **20**(1): p. 102-104.
- 42. Vijatović, M., J. Bobić, and B. Stojanović, *History and challenges of barium titanate: Part II.* Science of Sintering, 2008. **40**(3): p. 235-244.
- 43. Capurso, J.S., A.B. Alles, and W.A. Schulze, *Processing of laminated barium titanate structures for stress-sensing applications.* Journal of The American Ceramic Society, 1995. **78**(9): p. 2476-2480.
- 44. Yang, D., et al., *Dielectric elastomer actuator with excellent electromechanical performance using slide-ring materials/barium titanate composites*. Journal of Materials Chemistry A, 2015. **3**(18): p. 9468-9479.

- 45. Guo, J., et al., *Microwave Dielectric Ceramics Li2 MO 4– TiO2 (M= Mo, W) with Low Sintering Temperatures.* Journal of the American Ceramic Society, 2014. **97**(6): p. 1819-1822.
- 46. Barinova, O. and S. Kirsanova, *Moisture-sensitive ceramics of the Li 2 MoO 4-Li 2 WO 4 system.* Glass & Ceramics, 2008. **65**.
- 47. Kähäri, H., et al., *Room-temperature-densified Li2MoO4 ceramic patch antenna and the effect of humidity.* International Journal of Applied Ceramic Technology, 2017. **14**(1): p. 50-55.
- 48. Kähäri, H., et al., *Improvements and Modifications to Room-Temperature Fabrication Method for Dielectric Li 2 MoO 4 Ceramics.* Journal of the American Ceramic Society, 2015. **98**(3): p. 687-689.
- 49. Maria, J.-P., et al., *Cold sintering: current status and prospects.* Journal of Materials Research, 2017. **32**(17): p. 3205-3218.
- 50. Chen, H.-J. and Y.-W. Chen, *Hydrothermal synthesis of barium titanate*. Industrial & engineering chemistry research, 2003. **42**(3): p. 473-483.
- 51. Hakuta, Y., et al., *Continuous production of BaTiO3 nanoparticles by hydrothermal synthesis.* Industrial & engineering chemistry research, 2005. **44**(4): p. 840-846.
- 52. Nelo, M., et al., *Ultra-low permittivity ULTCC composite materials*. Applied Physics Letters, 2021. **118**(14): p. 142901.
- 53. Chen, J., et al., *Design and preparation of benzoxazine resin with high-frequency low dielectric constants and ultralow dielectric losses.* ACS Applied Polymer Materials, 2019. **1**(4): p. 625-630.
- 54. Rayssi, C., et al., Frequency and temperature-dependence of dielectric permittivity and electric modulus studies of the solid solution Ca 0.85 Er 0.1 Ti 1-x Co 4x/3 O 3 ( $0 \le x \le 0.1$ ). Rsc Advances, 2018. **8**(31): p. 17139-17150.
- 55. Yip, T.W., E.J. Cussen, and C. Wilson, *Spontaneous formation of crystalline lithium molybdate from solid reagents at room temperature*. Dalton Transactions, 2010. **39**(2): p. 411-417.
- 56. Wiederhorn, S., *Subcritical crack growth in ceramics*. Fracture Mechanics of Ceramics: Volume 2 Microstructure, Materials, and Applications, 1974: p. 613-646.
- 57. Berkowitz, B. and J. Zhou, *Reactive solute transport in a single fracture*. Water Resources Research, 1996. **32**(4): p. 901-913.
- 58. Osher, S. and R.P. Fedkiw, *Level set methods: an overview and some recent results.* Journal of Computational physics, 2001. **169**(2): p. 463-502.
- 59. Sethian, J.A. and P. Smereka, *Level set methods for fluid interfaces*. Annual review of fluid mechanics, 2003. **35**(1): p. 341-372.
- 60. Fei, F., et al., Study of Droplet Diffusion in Hydrothermal-Assisted Transient Jet Fusion of Ceramics. Journal of Manufacturing Science and Engineering, 2021. **143**(5): p. 051001.
- 61. Reaney, I.M. and D. Iddles, *Microwave dielectric ceramics for resonators and filters in mobile phone networks.* Journal of the American Ceramic Society, 2006. **89**(7): p. 2063-2072.
- 62. Gibson, I., et al., *Additive manufacturing technologies*. Vol. 17. 2021: Springer.

- 63. Mostafaei, A., et al., *Binder jet 3D printing—Process parameters, materials, properties, modeling, and challenges.* Progress in Materials Science, 2021. **119**: p. 100707.
- 64. Ren, L., X. Luo, and H. Zhou, *The tape casting process for manufacturing low temperature co-fired ceramic green sheets: a review.* Journal of the American Ceramic Society, 2018. **101**(9): p. 3874-3889.
- 65. Du, W., et al., *Ceramic binder jetting additive manufacturing: a literature review on density.* Journal of Manufacturing Science and Engineering, 2020. **142**(4): p. 040801.
- 66. Fei, F., et al., *Hydrothermal-assisted transient binder jetting of ceramics for achieving high green density.* JOM, 2020. **72**: p. 1307-1313.
- 67. Fei, F., et al., Study of Droplet Diffusion in Hydrothermal-Assisted Transient Jet Fusion of Ceramics. Journal of Manufacturing Science and Engineering, 2021. **143**(5).
- 68. Deckers, J., J. Vleugels, and J.-P. Kruth, *Additive manufacturing of ceramics: A review.*Journal of Ceramic Science and Technology, 2014. **5**(4): p. 245-260.
- 69. Bertrand, P., et al., *Ceramic components manufacturing by selective laser sintering.* Applied Surface Science, 2007. **254**(4): p. 989-992.
- 70. Tang, Y., et al., *Direct laser sintering of a silica sand*. Materials & design, 2003. **24**(8): p. 623-629.
- 71. Grau, J., et al. High green density ceramic components fabricated by the slurry-based 3DP process. in 1997 International Solid Freeform Fabrication Symposium. 1997.